Nanoscale

Accepted Manuscript

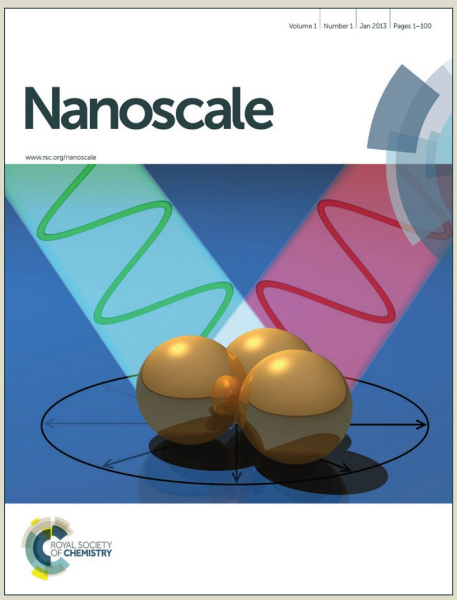

ROYAL SOCIETY OF CHEMISTRY

www.rsc.org/nanoscale

Quantitative characterization of conformational-specific protein-DNA binding using a dual-spectral interferometric imaging biosensor

Xirui Zhang[†], *George G. Daaboul*[†, ‡], *Philipp S. Spuhler*[†], *Peter Dröge*[§], *and M. Selim Ünlü*[†, ‡, *]

[†]Department of Biomedical Engineering, Boston University, Boston, Massachusetts, 02215, United States, [‡]Department of Electrical and Computer Engineering, Boston University, Boston, Massachusetts, 02215, United States, and [§]School of Biological Sciences, Nanyang Technological University, Singapore 637551

KEYWORDS: DNA bending, protein-DNA interactions, integration host factor, optical biosensor, DNA conformation, fluorescence vertical sectioning, DNA microarray

*Corresponding author: selim@bu.edu.

ABSTRACT

DNA-binding proteins play crucial roles in the maintenance and functions of the genome and yet, their specific binding mechanisms are not fully understood. Recently, it was discovered that DNA-binding proteins recognize specific binding sites to carry out their functions through an indirect readout mechanism by recognizing and capturing DNA conformational flexibility and deformation. High-throughput DNA microarray-based methods that provide large-scale protein-DNA binding information have shown effective and comprehensive analysis of protein-DNA binding affinities, but do not provide information of DNA conformational changes in specific protein-DNA complexes. Building on the high-throughput capability of DNA microarrays, we demonstrate a quantitative approach that simultaneously measures the amount of protein binding to DNA and nanometer-scale DNA conformational change induced by protein binding in a microarray format. Both measurements rely on spectral interferometry on a layered substrate using a single optical instrument in two distinct modalities. In the first modality, we quantitate the amount of binding of protein to surface-immobilized DNA in each DNA spot using a label-free spectral reflectivity technique that accurately measures the surface densities of protein and DNA accumulated on the substrate. In the second modality, for each DNA spot, we simultaneously measure DNA conformational change using a fluorescence vertical sectioning technique that determines average axial height of fluorophores tagged to specific nucleotides of the surface-immobilized DNA. The approach presented in this paper, when combined with current high-throughput DNA microarray-based technologies, has the potential to serve as a rapid and simple method for quantitative and large-scale characterization of conformational specific protein-DNA interactions.

INTRODUCTION

The maintenance and functions of the genome critically rely on specific protein-DNA interactions, which trigger and carry out essential molecular processes in the cell. Examples of such processes include DNA replication, DNA repair, gene expression and its regulation, genome rearrangement by DNA recombination and transposition, and DNA methylation[1-6]. How proteins specifically distinguish their specific binding site from the vast genomic nonspecific binding sites and subsequently execute their unique functions remains to be fully understood. In recent years, high-throughput DNA microarray-based methods, such as the protein-binding microarray (PBM) and high-throughput chromatin immunoprecipitation (HT-ChIP), have been proven to provide large-scale and comprehensive protein-DNA binding affinity information, important for the analysis of genetic regulatory networks and the effects of genetic variations on those networks[7-14]. For example, PBMs have enabled the analysis of the binding specificities of many transcription factors (TFs) to high-density, custom-designed microarrays of over 44,000 DNA spots containing all 10-mer sequence variants[9]. These approaches, which can obtain statistically meaningful results of protein-DNA interactions, do not provide information about the function and changes of DNA conformation in the formations of specific protein-DNA complexes. Recent findings suggest that DNA-binding proteins can achieve specific binding through an indirect readout mechanism by first binding nonspecifically and diffusing along the DNA sequence until they recognize, capture, or enhance specific DNA conformational fluctuations or deformations[6,15-20]. Therefore, to further the capability of these high-throughput approaches in understanding the mechanisms and biological functions of specific protein-DNA interactions, it is beneficial to obtain quantitative information about DNA conformational changes and their functions correlated with or caused by specific protein binding.

Here, we present a dual-mode imaging biosensor platform that enables quantitation of both DNA conformational changes and binding affinity of protein-DNA interactions in a DNA microarray format (Figure 1). The DNA conformational change induced by protein binding is measured by spectral self-interference fluorescence microscopy (SSFM), which determines surface-immobilized DNA conformation by measuring the average axial height of fluorophores tagged to specific nucleotides[21-25]. The amount of protein binding to surface-immobilized DNA is measured by white light reflectance spectroscopy (WLRS), which quantifies molecular surface densities via measuring surface-immobilized biomolecule layer thicknesses[22,26-30]. By implementing a dual-spectral imaging configuration, we can perform the two independent interferometric measurements simultaneously using two separate spectral ranges for multiple DNA spots simultaneously (Figure 1, See Experimental, Optical Setup).

To demonstrate simultaneous quantitation of protein-DNA binding and DNA conformational change, we use the integration host factor (IHF) protein of *Escherichia coli*, an architectural protein that induces a specific and functional bending of a 34-bp long dsDNA consensus sequence (Figure 1), as a molecular model system. In a specific IHF-DNA complex, IHF induces a sharp turn of the consensus sequence, facilitating many cellular processes, such as genetic recombination and transcriptional regulation, by apposing distant binding sites for other proteins[19,31-35]. Using WLRS to measure IHF-DNA binding, we can obtain information about the molecular surface density and ratio of IHF and surface-immobilized DNA specifically bound together. We then use this information and the average height changes of the fluorophores tagged to the dsDNA molecules measured by SSFM to precisely quantify DNA bending angle induced by specific IHF binding. The results for the IHF-DNA molecular model system demonstrate, as a proof of concept, that the imaging biosensor platform introduced in this paper can provide

previously inaccessible information regarding binding conformational specificity and affinity, and may open up new areas of exploration.

The major steps of our experimental approach are as follows: we first immobilize dsDNA molecules in a microarray format on a functionalized substrate and incubate the DNA microarray in a flow cell filled with buffer solution. The 5' end or the surface-proximal end of each dsDNA molecule is modified with an amine group to covalently anchor to the functionalized substrate whereas the 3' end or the surface-distal end of each dsDNA molecule is labeled with a fluorophore. We then use SSFM to measure the average axial height of the fluorophores at the surface-distal ends of the immobilized dsDNA molecules and use WLRS to measure the average surface density of the dsDNA molecules in each DNA spot. We subsequently introduce a binding solution containing IHF molecules and allow IHF binding to the surface-immobilized dsDNA molecules to reach equilibrium. We then take a second, post-binding SSFM measurement to measure the average axial height of the fluorophores again to quantify DNA conformational changes. We also take a second, post-binding WLRS measurement to measure the average surface density of IHF molecules bound to each DNA spot. The results obtained using the combination of SSFM and WLRS allow quantitative analysis of IHF-DNA binding and the specific DNA conformational changes induced by IHF binding.

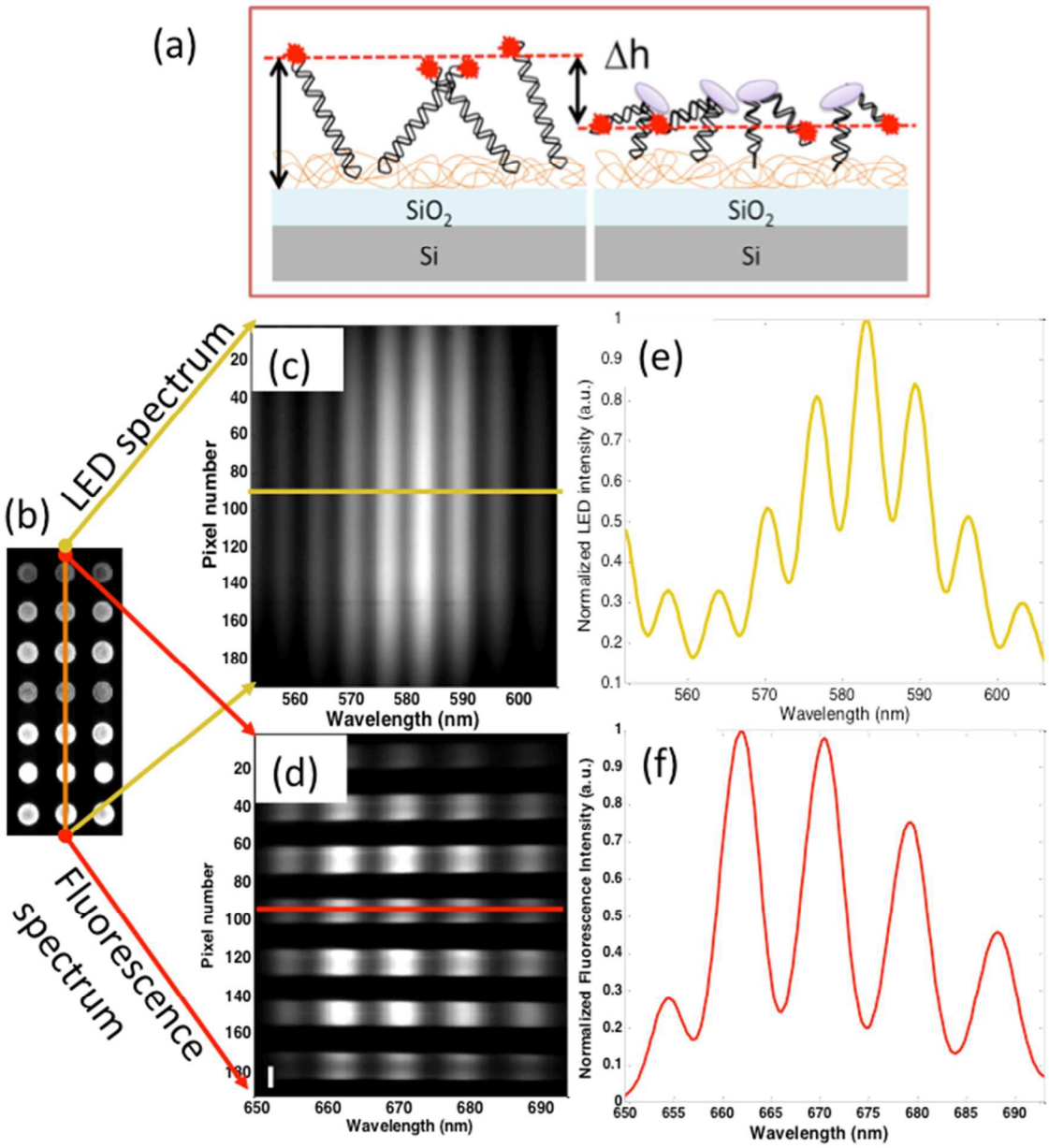

Figure 1. High-throughput imaging biosensor combining SSFM and WLRS for simultaneous quantitation of conformational specificity and binding affinity of specific protein-DNA interactions. (a) The underlying principles of quantifying both DNA conformational change and DNA-protein binding affinity on a DNA microarray surface. The microarray substrate is functionalized with a polymeric coating (orange matrix) to form covalent bonds with DNA molecules modified with amine groups at the surface-proximal ends. The surface-distal ends of

surface-immobilized DNA molecules are labeled with ATTO647N (red) fluorophores. The thickness of the DNA spot on the surface is measured by WLRS and used for obtaining the average surface density of the DNA molecules in each DNA spot. (b) A fluorescence image of a sample DNA microarray on a polymer-functionalized substrate acquired by GenePix® 4000B Microarray Scanner (Molecular Devices, LLC, Sunnyvale, CA). The orange line indicates that an image of a slit in front of an LED light source of the WLRS setup and a line of the laser of the SSFM setup overlap and are focused on a line of DNA spots at the center. (c) A one-dimensional (1-D) spectral image of an image of the LED slit focused on the microarray substrate. (d) A 1-D spectral image of the excited DNA spots by the line of laser focused on the microarray substrate. (e) A sample LED interference spectrum averaged over 10 pixels at the center of one DNA spot, indicated by the yellow horizontal line in (c). (f) A sample fluorescence interference spectrum integrated over 10 pixels at the center of one DNA spot, indicated by the red horizontal line in (d).

RESULTS AND DISCUSSION

DNA Sequence Design. To demonstrate the capabilities of the imaging biosensor platform, we designed three 60-bp IHF-binding DNA sequences containing a 34-bp H′ site of bacteriophage λ, one of the best-characterized IHF consensus binding sites[31,32,34]. We designated the H′ site to start at three different nucleotide positions along the 60-bp DNA sequences, which we indicated by adding the starting nucleotide position in a parenthesis in the names of the DNA sequences. Given that the 60-bp dsDNA molecules are end-tethered and oriented on a surface[36-38], a smaller starting nucleotide position of the H′ site results in a shorter distance of the H′ binding site to the surface. We also designed an arbitrary 60-bp control sequence without the H′ site. The control

sequence was designed to have a 50% GC content and minimized secondary structures using Oligo Analyzer (Integrated DNA Technologies, Inc., Coralville, IA). Further, we designed another sequence with a single nucleotide mutation to one of the 60-bp IHF-binding sequences possessing the H′ site. The mutated sequence had a T replaced by an A in the consensus TTR element, which was previously shown to disturb the stabilizing electrostatic interactions between the IHF side chain and the dsDNA molecule[39,40]. The full list of the DNA sequences used in the experiments can be found in Table 1S in the Supporting Information.

Simultaneous detection of IHF binding and binding-induced dsDNA bending at equilibrium. We performed end-time equilibrium measurements of IHF binding to the 60-bp IHF-binding sequence H′ (39) and the control sequence at a series of IHF concentrations ranging from 0 to 40 nM (Figure 2). The DNA microarray spots of the two sequences were consecutively incubated in a customized flow cell with binding buffer solutions containing IHF at a range of concentrations. The binding buffer solutions were constantly driven through the flow cell at a flow rate of 500 μL/min. More details of the flow cell design and the experimental procedure are described in section 5 in the Supporting Information and Experimental Section. End-time equilibrium binding isotherms of both fluorophore height change and IHF accumulation were obtained by averaging measurements of ten dsDNA spot replicates of each sequence.

Figure 2(a) shows the average IHF to DNA molecular binding ratios of 10 dsDNA spot replicates at increasing concentrations of IHF at equilibrium. The IHF to DNA binding ratio of each DNA spot was calculated by dividing the measured ensemble average surface density of the bound IHF by the measured ensemble average surface density of dsDNA in a measured area of the DNA spot at equilibrium, which were quantitated by WLRS. WLRS has previously been shown to quantify the surface density of surface-immobilized DNA and protein molecules[41,42]. A

summary of the average surface densities of dsDNA and bound IHF for each DNA sequence is included in Table 4S in the Supporting Information. As shown in Figure 2(a), the error bars of the average IHF to DNA binding ratio results are relatively large. Each error bar of the average IHF to DNA binding ratio is the standard deviation of the average IHF to DNA binding ratios of 10 DNA spots. Because the ratio is derived from two variables, the standard deviation of the ratio reflects the sum of the variations of two variables. Moreover, as discussed in the Supporting Information, the surface density of the immobilized DNA molecules of the DNA spots can affect the amount of IHF bound to the DNA spots. Thus, the variance of the surface densities of different DNA spots can contribute to the variance in the amount of bound IHF, and then translate to greater amount of variance in the calculated average IHF to DNA binding ratio. The error bars or standard deviation of the IHF to DNA binding results can be reduced in future experiments. For example, the error bars or the standard deviations of the measured results can be reduced by measuring more DNA spots and by reducing the variability of the surface densities of different DNA spots.

Figure 2(b) shows the average height changes of the surface-distal end fluorophores of the 10 dsDNA spots at increasing concentrations of IHF at equilibrium. To obtain the dissociation constants, K_d, for IHF binding to the two DNA sequences, H′ (39) and the control sequence, at first, we used nonlinear Least Squares Fitting to fit each equilibrium binding isotherm to an adapted Langmuir binding isotherm, which describes the relationship between the fraction of occupied ligand-binding sites to unbound ligand concentration[43,44]. From the nonlinear Least Squares Fitting, we also obtained the maximum average fluorophore height change at equilibrium, $\langle \Delta h_{max} \rangle$, and the maximum average IHF to DNA binding ratio at equilibrium,

$\langle R_{max} \rangle$. Details for analyzing the equilibrium binding isotherms to obtain these fitting parameters can be found in section 4 in the Supporting Information.

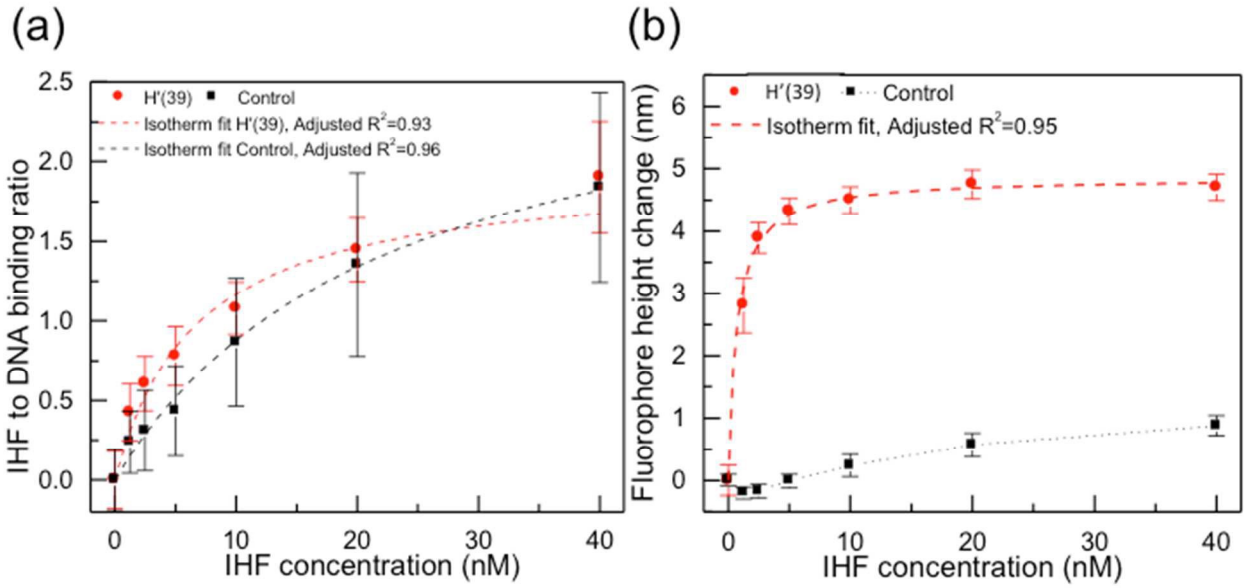

Figure 2. Equilibrium binding isotherms of IHF to DNA for DNA sequence H′(39) and the control sequence measured by WLRS and SSFM. (a) Average IHF to DNA binding ratios of 10 DNA spot replicates at different IHF concentrations by WLRS. (b) Average fluorophore height changes of the same set of DNA spot replicates at different IHF concentrations by SSFM. Dotted lines are fitting models as discussed in the main text and in the Supporting Information.

The fluorophore height changes measured by SSFM and the IHF to DNA binding ratios measured by WLRS were simultaneous measurements of the same binding assay. However, as illustrated by the experimental data shown in Figure 2, it is evident that the two equilibrium binding isotherms are significantly different. Previous studies have shown that IHF functions in both specific and nonspecific binding complexes and its concentration and binding specificity vary with cell growth[33,45]. In nonspecific binding, IHF can bind to a 9 to 16-bp long DNA and act as one of the major nucleoid-associated proteins to compact the 4.7 million-bp circular DNA into

the bacterial chromatin[45,46,33]. Since IHF have both specific and nonspecific binding modes[32,33,47,46], we hypothesize that the average IHF to DNA binding ratios measured by WLRS were contributed by both specific binding and nonspecific binding of IHF whereas the average fluorophore height changes measured by SSFM were only contributed by dsDNA bending caused by specific binding of IHF. We thus further assume that the K_d obtained from the equilibrium binding isotherm of fluorophore height changes due to DNA bending characterizes specific binding of IHF to DNA and is thus designated as $K_{d(specific)}$. This assumption is supported by the measurement of the nonspecific control sequence, which showed no fluorophore height change or DNA bending (Figure 2(b)).

To decouple the contributions of specific and nonspecific binding to the IHF to DNA binding ratios measured by WLRS, we fit the equilibrium binding isotherm of the average IHF to DNA binding ratios to an additive model that adds two adapted Langmuir binding isotherms, one describing specific binding of IHF to dsDNA, the other describing nonspecific binding of IHF to DNA. Detailed description of the additive model and the fitting and can be found in the Experimental Section and section 4 in the Supporting Information. From fitting the equilibrium binding isotherms of average IHF to DNA binding ratio to the additive model, we then obtained the maximum average binding ratios of IHF to the DNA sequences at equilibrium for both specific and nonspecific binding, $\langle R_{specific} \rangle$ and $\langle R_{nonspecific} \rangle$, and the dissociation constant of nonspecific IHF binding to the DNA sequences, $K_{d(nonspecific)}$, as shown in Table 1. Because WLRS quantitates ensemble average surface density of the measured dsDNA molecules in each DNA spot, $\langle R_{specific} \rangle$ can be interpreted as the maximum average ratio of the number of IHF molecules specifically bound to the measured dsDNA molecules at equilibrium, and $\langle R_{nonspecific} \rangle$ can be interpreted as the maximum average ratio of the number of IHF molecules

nonspecifically bound to the measured dsDNA molecules at equilibrium. Alternatively, $\langle R_{specific} \rangle$ can be interpreted as the maximum average number of IHF molecules specifically bound to each dsDNA molecule measured, and $\langle R_{nonspecific} \rangle$ can be interpreted as the maximum average number of IHF molecules nonspecifically bound to each dsDNA molecule measured in each DNA spot. The dissociation constant for specific IHF binding, $K_{d(specific)}$, was obtained from the average fluorophore height changes measured by SSFM. The value of $K_{d(specific)}$ of IHF binding sequence H'(39) agrees with the typical range of 0.5 to 20 nM for the dissociation constant of IHF binding to the 34-bp H' consensus sequence[33,48].

Table 1. Binding parameters obtained from equilibrium measurements of average IHF to DNA binding ratios and average fluorophore height changes for DNA sequence H'(39) and control sequence.

DNA	$\langle \Delta h_{max} \rangle$ (nm)	$\langle R_{specific} \rangle$	$K_{d(specific)}$ (nM)	$\langle R_{nonspecific} \rangle$	$K_{d(nonspecific)}$ (nM)
H'(39)	4.9 ± 0.1	0.54 ± 0.02	0.7 ± 0.1	2.6 ± 0.1	35.7 ± 4.2
Control	NA	NA	NA	2.6 ± 0.5	22.2 ± 6.4

Now, we can use the binding parameters in Table 1 to calculate the bending angle of dsDNA caused by specific IHF binding. Since SSFM measures ensemble average of the axial heights of the fluorophores tagged to dsDNA molecules within a focused region, such as the diffraction limit of the optical setup, the measured fluorophore height change after IHF binding is an ensemble average, including both unbent dsDNA molecules and bent dsDNA molecules caused by specific IHF binding within the region. Not knowing about the ratio between the bent and unbent dsDNA molecules may prevent an accurate calculation of the bending angle of the bent

dsDNA molecules caused by specific IHF binding based on the ensemble average measurement of SSFM.

However, by combining WLRS to SSFM, average IHF to DNA specific binding ratio can be obtained from the WLRS measurement. The average IHF to DNA specific binding ratio can then be used to normalize the ensemble average of fluorophore height changes to obtain the average fluorophore height changes of just the bent dsDNA molecules. We used a geometric model to calculate the average bending angle of dsDNA molecules induced by specific IHF binding using the average fluorophore height changes of the specifically bent DNA molecules. The average bending angle of dsDNA sequence H′(39) caused by IHF specific binding was calculated to be 162.4° with a standard deviation of 11.3°. The calculated average dsDNA bending angle agrees with the dsDNA bending angles measured by other methods, such as gel electrophoresis and X-ray crystallography[31], which range from about 120° to about 180°. More details for the geometric model for quantitation of dsDNA bending angle induced by specific IHF binding can be found section 5 in the Supporting Information. Our results demonstrate that the simultaneous detection of IHF-DNA binding by combining WLRS and SSFM can accurately and conveniently determine the dsDNA bending angle caused by specific IHF binding.

The geometric model we used for calculating dsDNA bending angle induced by IHF may not necessarily reflect the complete IHF binding induced dsDNA bending mechanism, in which IHF binding causes two kinks of the dsDNA helix, resulting in the overall bending, as previously shown by X-ray crystallography studies[31]. Additionally, the geometric model may not be universally applicable for analyzing all protein-DNA complexes. However, we may still use the model or measurements of fluorophore height changes for preliminary assessment of protein-DNA interactions, whose conformational change mechanisms remain to be discovered and

studied. For example, different DNA bending angles obtained or different average fluorophore height changes detected by SSFM may suggest different binding mechanisms or binding site locations, and precise structural and mechanistic examinations of interested protein-DNA interactions can be further obtained by other methods, such as X-ray crystallography and NMR.

Distinguishing 2-bp shifts of the IHF consensus binding site from measurements of DNA specific conformational changes. Given a certain dsDNA length longer than the H' consensus binding site, as shown in Figure 3(a), the dsDNA sequence having the H' binding site at a lower location would have a larger fluorophore height change resulted from a similar IHF-induced dsDNA bending. This idea of distinguishing protein-binding site locations on DNA sequences by detecting fluorophore height changes was previously tested on the "Switching-DNA" platform, which showed that the fluorescence intensity after IHF binding decreased as the H' binding site on 80-bp dsDNA molecules shifted closer to the surface[49]. However, the "Switching-DNA" platform, relying on normalized fluorescence intensity measurements, cannot provide accurate measurements of fluorophore height changes or specific dsDNA bending angles. As shown previously, our high-throughput imaging biosensor combining WLRS and SSFM enables simultaneous quantitative examination of IHF-DNA binding and fluorophore height changes resulted from DNA bending. We thus demonstrate distinguishing shifted H' binding site locations on 60-bp DNA sequences on our imaging biosensor platform.

We compared average fluorophore height changes of DNA sequences H′(34), H′(36), and H′(39), in which numerical notation indicates the center location of the H′ binding site along the DNA sequence respectively as described above. We observed different equilibrium binding isotherms of average fluorophore height changes of the three DNA sequences as expected (Figure 3(b)). As can be seen in Figure 3(b), the average fluorophore height change of DNA

sequence H′(34) was larger than that of DNA sequence H′(36), both of which were larger than that of DNA sequence H′(39) (Figure 3(c)). We then fit the equilibrium binding isotherm of the average fluorophore height change to a single adapted Langmuir binding isotherm model to obtain the maximum average fluorophore height change, $\langle \Delta h_{max} \rangle$, and the dissociation constant for specific IHF binding, $K_{d(specific)}$, for each DNA sequence as discussed above. We also fit the equilibrium binding isotherm of the average IHF to DNA binding ratio to the additive model for each DNA sequence, and obtained the maximum average binding ratios of IHF to each DNA sequence at equilibrium for both specific and nonspecific binding, $\langle R_{specific} \rangle$ and $\langle R_{nonspecific} \rangle$, and the dissociation constant of nonspecific IHF binding to the DNA sequences, $K_{d(nonspecific)}$. The obtained binding parameters for the three sequences are shown in Table 2 below.

Table 2. Binding parameters obtained from fitting equilibrium measurements of average IHF to DNA binding ratios and average fluorophore height changes for DNA sequences, H'(39), H'(36) and H'(34).

DNA	$\langle \Delta h_{max} \rangle$ (nm)	$\langle R_{specific} \rangle$	$K_{d(specific)}$ (nM)	$\langle R_{nonspecific} \rangle$	$K_{d(nonspecific)}$ (nM)
H'(39)	4.9 ± 0.1	0.54 ± 0.02	0.7 ± 0.1	2.6 ± 0.1	35.7 ± 4.2
H'(36)	5.5 ± 0.1	0.44 ± 0.04	0.6 ± 0.1	2.2 ± 0.3	24.7 ± 6.8
H'(34)	6.3 ± 0.1	0.38 ± 0.04	0.7 ± 0.1	1.8 ± 0.3	36.8 ± 11.3

As mentioned above, SSFM measures ensemble average fluorophore height changes of the dsDNA molecules resided in a measured area within a DNA spot. Thus, the measured fluorophore height change of each DNA spot is an ensemble average of the fluorophore height changes of both specifically bent and unbent DNA molecules. Because the IHF to DNA specific

binding ratio, $\langle R_{specific} \rangle$, indicates the amount of dsDNA molecules specifically bent by IHF of the total amount of dsDNA molecules measured, we thus further normalized the maximum average fluorophore height change, $\langle \Delta h_{max} \rangle$, by the average IHF to DNA specific binding ratio, $\langle R_{specific} \rangle$, of each DNA sequence. Such normalization allows for the examination of the fluorophore height changes of only the specifically bent DNA molecules, and thus leads to more accurate calculation of the bending angles of the specifically bent DNA molecules. By this normalization, we also obtained even greater distinction between the three DNA sequences (Figure 3(c)). Additionally, variability of the surface-immobilized dsDNA molecules of the three DNA sequences may affect the distinction between these sequences. For example, lower binding site locations and higher surface densities of the dsDNA molecules may reduce the accessibility of the binding site to the IHF molecules in solution, and may increase the steric hindrance for the specific bending of the dsDNA molecules. Such variability can inhibit IHF specific binding, which can eventually affect the average IHF to DNA specific binding ratio, $\langle R_{specific} \rangle$, of each DNA sequence, and reduce the ensemble average fluorophore height changes measured by SSFM. Therefore, the normalization of the maximum average fluorophore height change, $\langle \Delta h_{max} \rangle$, by the average IHF to DNA specific binding ratio, $\langle R_{specific} \rangle$, for each DNA sequence decouples the effect of the variability of IHF to DNA binding ratios between the DNA sequences due to changes of the binding site locations and surface densities. This experiment proves that our high-throughput imaging biosensor can quantitatively distinguish as small as 2-bp shifts of the 39-bp H′ binding site location along 60-bp DNA sequences. We further examine and discuss the effects of surface density and binding site location on the specific binding of IHF and the specific bending angles of the dsDNA moelcules for the three DNA sequences in section 10 in the Supporting Information.

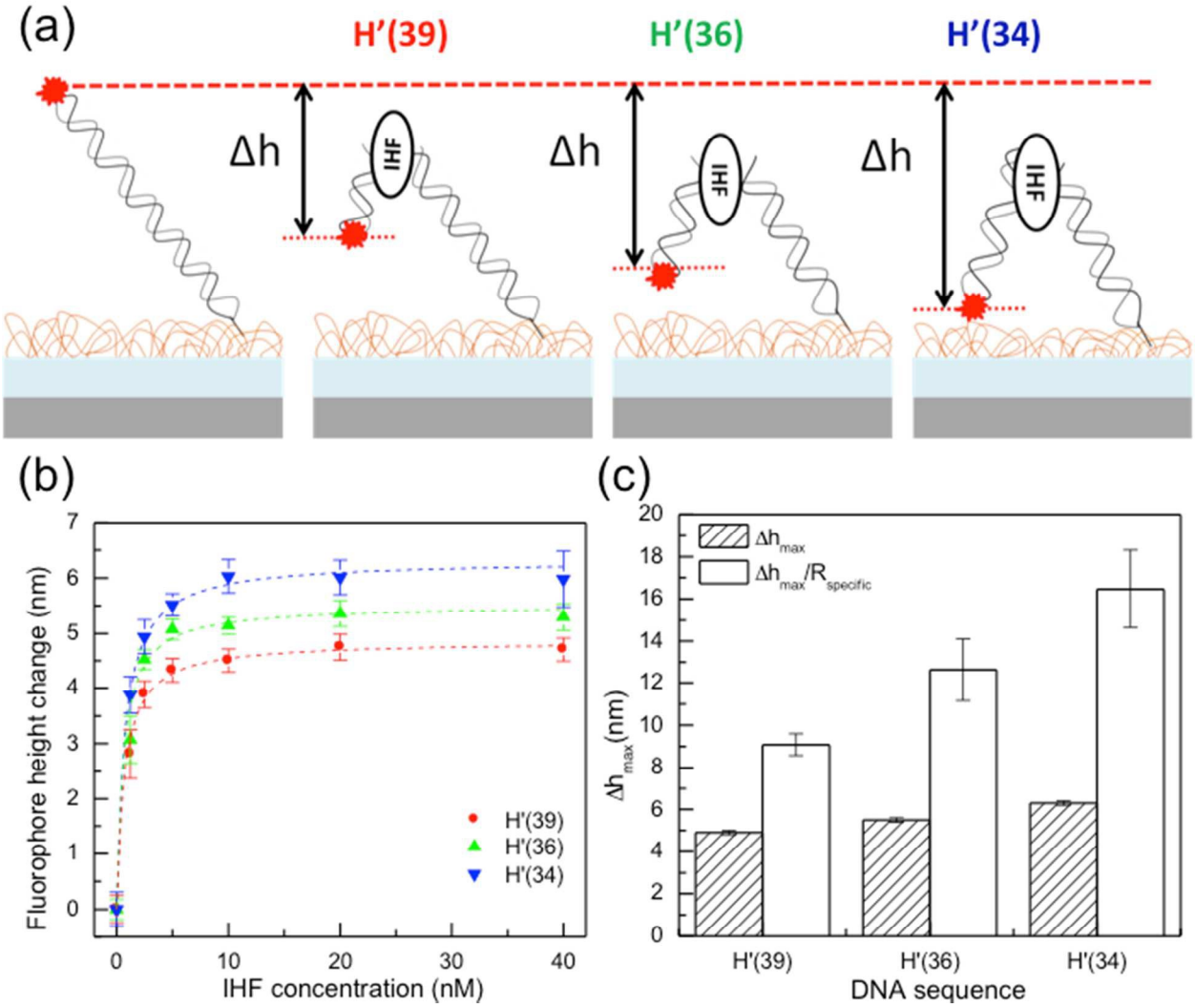

Figure 3. Distinguishing shifted H′ binding site locations. (a) The H' binding site positioned at a lower location along an IHF-binding sequence supposedly results in a larger fluorophore height change due to IHF-induced DNA bending. (b) Equilibrium binding isotherms of average fluorophore height changes of three DNA sequences, H′(34), H′(36), and H′(39). (c) Compare maximum average fluorophore height changes, $\langle \Delta h_{max} \rangle$, and maximum average fluorophore height changes, $\langle \Delta h_{max} \rangle$, normalized by average IHF to DNA specific binding ratio, $\langle R_{specific} \rangle$, among the three DNA sequences. Differentiation among the three DNA sequences becomes more evident after the normalization.

Distinguishing single nucleotide mutation from the detection of DNA conformational changes. Studies have shown that a single T to A mutation in the center of the TTR consensus element of the H' binding site can destabilize the IHF-DNA complex[39,40]. As part of its indirect readout mechanism, IHF distinguishes this mutation by recognizing the different flexibility of the YpR step, which disturbs stabilizing electrostatic interactions between the IHF side chain and the dsDNA[39,40]. By detecting conformational specific binding, we demonstrate discrimination of IHF-binding sequence with a single nucleotide mutation using our imaging biosensor platform.

First, we acquired the equilibrium binding isotherms of average fluorophore height changes and average IHF to DNA binding ratios of IHF-binding DNA sequence, H'(34), a DNA sequence, H'(34)A, with a single nucleotide mutation, and the arbitrary control sequence as discussed previously. The results in Figure 4 similarly show the average and standard deviation of measurements of 10 DNA spot replicates. According to the quantitative analysis of the equilibrium binding isotherms described previously, we obtained the specific binding dissociation constant $K_{d(specific)}$ and the maximum average fluorophore height change, $\langle \Delta h_{max} \rangle$, for both sequences. We also fitted the equilibrium binding isotherms of IHF to DNA ratios to the additive Langmuir model. Additionally, we calculated and compared the specific dsDNA bending angles of the two DNA sequences. The obtained the fitting parameters and calculated bending angles are presented in Figure 4 and Table 3 below.

As shown in Figure 4(a) and Figure 4(b), SSFM can positively detect the mutated sequence from the difference of average fluorophore height changes measured at equilibrium in 40 nM IHF solution while mass density measurements by WLRS cannot. In Table 3, we compare $K_{d(specific)}$ and calculated average dsDNA bending angle of the two DNA sequences, H'(34) and H'(34)A. We observed that the $K_{d(specific)}$ of H'(34)A was about three times of that of H'(34)

under our experimental conditions and $K_{d(nonspecific)}$ of H'(34)A was about twice of that of H'(34). We also observed that the dsDNA bending angle induced by IHF binding of H'(34)A was slightly smaller than that of H'(34). These results suggest that IHF are more tightly bound to DNA sequence H'(34) that includes the consensus binding element than DNA sequence H'(34)A that includes the consensus binding element with a single nucleotide mutation, which agrees with previous published studies.

Table 3. Binding parameters obtained from fitting equilibrium measurements of average IHF to DNA binding ratios and average fluorophore height changes.

DNA	$\langle \Delta h_{max} \rangle$ (nm)	$\langle R_{specific} \rangle$	$K_{d(specific)}$ (nM)	$\langle R_{nonspecific} \rangle$	$K_{d(nonspecific)}$ (nM)	Bending Angle (º)
H'(34)	6.3 ± 0.1	0.38 ± 0.04	0.7 ± 0.1	1.8 ± 0.3	36.8 ± 11.3	150.6 ± 12.1
H'(34)A	4.4 ± 0.1	0.55 ± 0.03	1.8 ± 0.2	2.7 ± 0.4	71.4 ± 17.5	124.2 ± 26.2

The dissociation constant, $K_{d(specific)}$, of specific binding of IHF to the mutant sequence H'(34)A obtained from conformational detection was smaller than previous EMSA results[39]. We attribute this difference to the respective binding environment and specific detection methodology used for obtaining the result. While EMSA measurements were made in non-equilibrium conditions and conformational variation could affect shifts of protein-DNA complexes in the gel, SSFM measurements were made at equilibrium to specifically detect dsDNA conformational changes.

Interestingly, our results further indicate that the average bending angle of the mutated DNA sequence H'(34)A is just slightly smaller than DNA sequence H'(34), which contains the H'

consensus binding site. This result agrees with and further supports previous studies of the X-ray crystal structure of the binding complex comprising IHF and the single-nucleotide mutated H' binding site, which did not report significant difference of the DNA bending angle from the IHF-H' complex[39]. The observed slightly smaller average bending angle of the mutated H' sequence in our results further suggests that the mutated H' sequence may still substantially bend upon binding to IHF, and this bent structure may fluctuate from a tightly wrapped structure of the original IHF-H' complex. This agrees with a recent study suggesting that the single T to A mutation does not affect the bendability of the DNA at the kinks[19].

As demonstrated above, the high-throughput imaging biosensor platform presented in this paper has the potential to enable effective and comprehensive simultaneous analysis of protein-DNA binding affinities as well as conformational specificity. For example, the imaging biosensor platform can be combined with high-throughput protein-binding microarrays (PBMs) to quantitatively characterize DNA sequence specificities of transcription factors to obtain conformational, functional, and regulatory insights of transcription factors and their binding sites[7,50-52]. Additionally, WLRS is a label-free method for quantitation of the amount of protein and DNA accumulated on the substrate and SSFM only requires the DNA molecules to be labeled with fluorophores. Thus, the protein molecules to be studied do not need to be tagged or labeled with fluorophores. This allows the protein molecules to interact with their binding sites in their native structures and simplifies the binding assay.

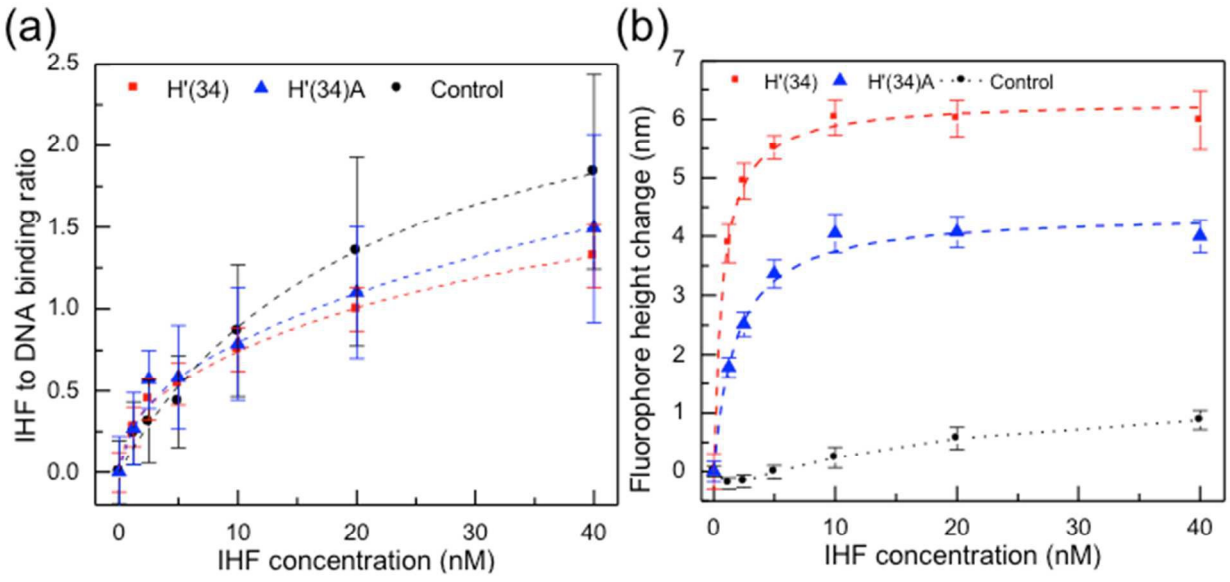

Figure 4. Detection of single nucleotide mutation of IHF consensus binding sequence. (a) Equilibrium binding isotherms of average IHF to DNA binding ratios of IHF-binding sequence H'(34), IHF-binding sequence with a single mutation H'(34)A, and a control sequence. (b) Equilibrium binding isotherms of average fluorophore height changes of the three DNA sequences.

EXPERIMENTAL

1. Optical setup

Spectral Self-interference Fluorescence Spectroscopy (SSFM, Figure 5~~Figure 5~~). In the excitation path, helium-neon laser with peak intensity at 633 nm (Melles Griot, Carlsbad, CA) was collimated and expanded with two achromatic lenses with respective focal lengths of 30 mm and 150 mm (Thorlabs Inc., Newtown, NJ). The on-and-off of the laser was controlled by a mechanical shutter that opens and closes via a transit voltage signal (+5V or 0V). A dual-edge dichroic beam splitter (545/650 nm BrightLine, Semrock, Inc. NY) that specifically reflects the

wavelength of the laser and transmits >90% of the fluorescence emission of ATTO647N (red fluorophore) directed the collimated laser beam to the objective. Before the beam splitter reflected the collimated beam, a cylindrical lens focused the circular laser beam to a line at the back focal plane of the objective. The objective (Nikon 5x, numerical aperture (NA) = 0.13) then performed Fourier Transform of the laser line beam and focused the laser line beam to a diffraction-limited line in the other dimension on the biosensor surface. In the collection path, the excited line of fluorescence emission on the surface was imaged onto the entrance slit of a spectrometer (SP-2150i, Princeton Instruments, Trenton, NJ) by using the same objective, another beam splitter (92% reflection, 8% transmission), and a tube lens. A two-dimensional (2-D) CCD camera (PIXIS 256E, dimensions 26 mm x 6.7 mm, 1024 x 256, 26 μm x 26 μm pixels, Princeton Instruments, Trenton, NJ) was connected to the spectrometer to collect the image of the excited line of fluorescence emission in the vertical dimension and the fluorescence interference spectra in the horizontal dimension. The bright pixels imaged in the vertical dimension matched the position and size of each DNA spot in the line image. Thus, a 1-D spectral image acquired by the CCD camera of the fluorescence emission of multiple DNA spots along the line on the surface was then saved for spectral fitting and analysis.

White Light Reflectance Spectroscopy (WLRS, Figure 5**)** In the illumination path, a wide-band yellow LED (M565L2, Thorlabs, Newton, NJ) was used as the illumination source. A rectangular slit 100 μm wide and 3 mm tall (S100R, Thorlabs, Newton, NJ) was placed in front of the LED on a rotation mount (CRM1, Thorlabs, Newton, NJ). An image of the slit was focused and superimposed on the focused laser line on the biosensor surface using a 50:50 beam splitter (Thorlabs, Newton, NJ) and the same objective. A relay lens on an x, y translation mount (CXY1Q, Thorlabs, Newton, NJ) was placed in front of the rectangular slit at a position where

the LED slit image had the same focus with the laser line. Precise alignment of the position and orientation of the slit image with those of the laser line was made by tuning the x and y position of the translation mount and the rotation mount while examining their positions in real time on a CMOS camera (ORCA-Flash2.8 C11440-10C Digital CMOS camera, Hamamatsu, Japan) at a height above the objective. Focusing of the laser line and the LED slit image on the biosensor surface was also achieved by observing their images on the CMOS camera and adjusting the distance of the biosensor surface to the objective. Since the power of the LED was far more sufficient, the reflection/transmission passband of beam splitters were selected to maximize the fluorescence collection efficiency. In the collection path, the LED slit image was then imaged in the same fashion as the excited line of fluorescence emission onto the entrance slit of the spectrometer. The 1-D spectral image acquired by the CCD camera of the LED slit image on the biosensor surface was also saved for spectral fitting and analysis.

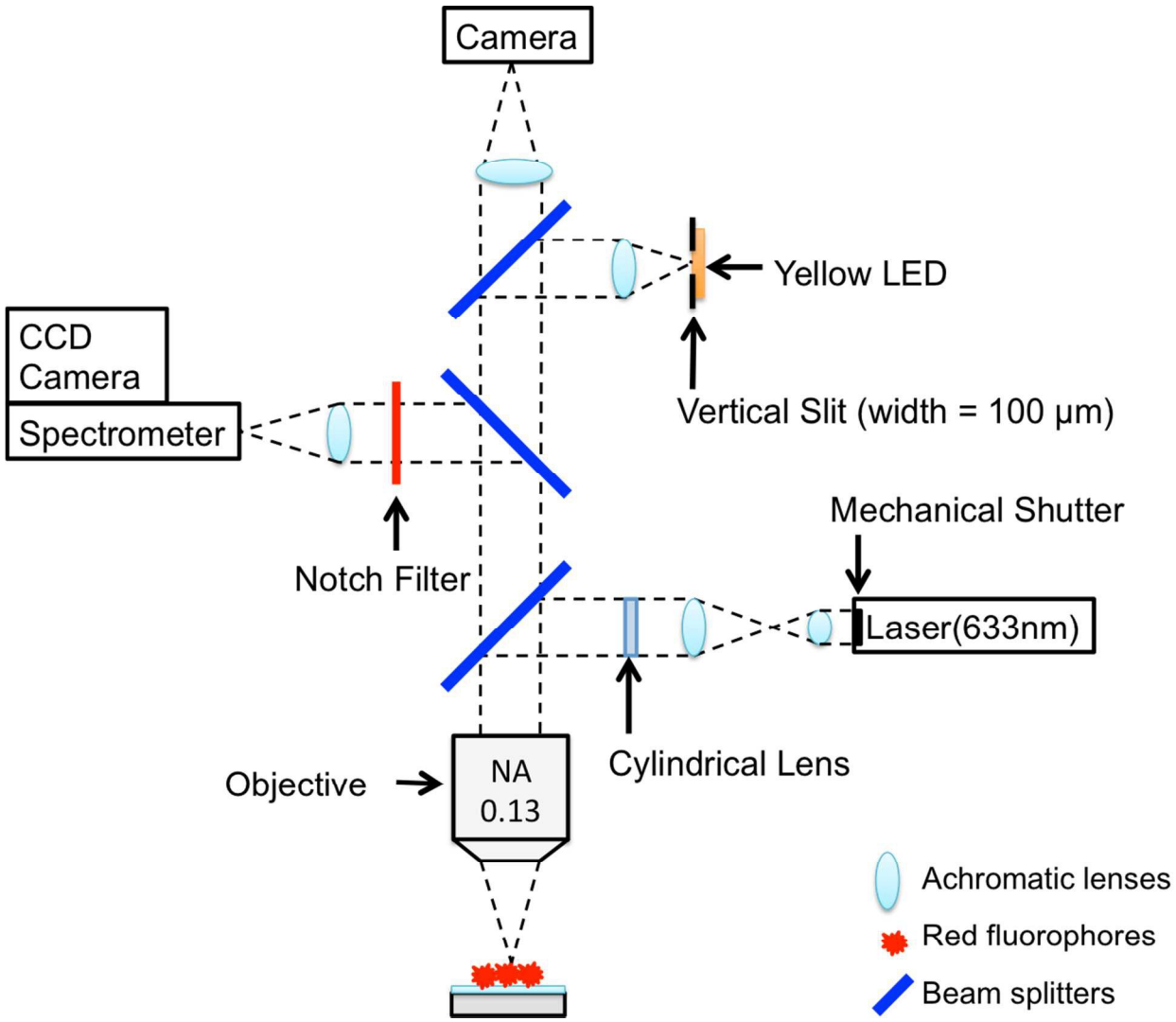

Figure 5. Schematic illustration of the optical setup of the high-throughput imaging biosensor combining Spectral Self-interference Fluorescence Microscopy (SSFM) and White Light Reflectance Spectroscopy (WLRS). Components are not to scale.

Microarray scanning and spectral analysis. The biosensor substrate was placed in a custom flow cell fixed on a 4-axis stage that consists of an x, y translation micro-stage (Mad City Labs, Madison, WI), a manual z translation stage, and a 360° high-precision rotation mount (PR01, Thorlabs, Newton, NJ). The z translation was for fine focusing of the laser and LED slit image, the rotation mount was for DNA microarray alignment in the x, y direction, and the x, y

translation was for DNA microarray scanning. To perform automatic spectrum measurement of the DNA microarray, an in-house written MATLAB software application controlled and coordinated the spectrometer acquisition, the micro-stage movement, the laser shutter, and the LED.

The number of DNA spots that can be measured at the same time depends on the 1-D imaging field of view of the spectrometer and the size and pitch of the DNA spots. The dimensions of the CCD camera of the spectrometer and the magnification of the objective determined the field of view. The current 1-D imaging configuration allows a total of 7 DNA spots to be measured at the same time. The total amount of time required to scan the whole DNA microarray depends on the number of DNA spots per measurement, the total number of DNA spots in the microarray, and the time required for each measurement. Taking the current 1-D spectral imaging system for an example, each measurement takes about 0.1 to 0.5 second and each measurement covers 7 DNA spots, plus additional time used for translating the stage (on the scale of milliseconds per translation, e.g., 0.5 second) and for switching on and off the illumination source between two measurements. Thus, currently the scanning a total of 750 spots can take about less than 4 minutes. Using a larger CCD sensor array and an objective of smaller magnification, or performing 2-D spectral imaging can further increase the number of DNA spots that can be imaged and measured simultaneously.

To find the centers of DNA spots, as shown in Figure 1, a series of fluorescence spectral images were acquired by scanning from one edge of the DNA spots to the other. The middle position between the edges was determined to be the center of that line of DNA spots. The center positions of other lines of DNA spots in the microarray were calculated from the determined position of the line of DNA spots and the microarray pitch distance. The line of excited

fluorescence emission and the LED slit image on the biosensor surface were both imaged onto spectrometer CCD camera of the spectrometer (Figure 1). The pixel number on the vertical axis corresponds to a unique position along the imaged line on the surface. The number of pixels spanned by each DNA spot can be approximated by 120 μm (spot diameter) × 4.17 (magnification) /26 μm (CCD pixel size) = 17 pixels. The fluorescence interference spectrum was integrated over 10 pixels at the center of each DNA spot to obtain sufficient SNR for fitting. The LED interference spectrum for each pixel along the line of the slit image was fit to obtain a thickness measurement. A moving average filter using a window length of 5 pixels was used to reduce the random noise and reveal thickness step changes. Background thickness measurements for the determination of DNA spot thicknesses were made separately at a middle position between the lines of DNA spots. The DNA spot positions were visible along the vertical axis of the fluorescence spectral image, but were indistinguishable from nearby background in LED spectral image. However, we can assume the position of each DNA spot in the LED spectral image is the same as that in the fluorescence spectral image. This is because the focused LED slit image was carefully aligned and superimposed with the focused laser line on the biosensor surface. Finally, the LED and fluorescence interference spectra along the horizontal axis in the spectral image of each DNA spot were fit with custom algorithms using MATLAB.

2. Materials and binding experiments.

Single-stranded 60-bp DNA molecules were purchased from IBA GmbH (Goettingen, Germany). All ssDNA molecules were purified with high-performance liquid chromatography (HPLC) after synthesis. For DNA surface immobilization, the first strand was modified with an amine-C6 linker on the 5’ end while its complementary strand was modified with an Atto647N fluorophore on the 5’ or 3’, corresponding to either the surface-distal end or surface-proximal

end on hybridized dsDNA immobilized on the polymer functionalized surface. We selected Atto647N fluorophore to label the DNA strands because of its superior photostability than other organic dyes. The fluorescence emission spectrum of Atto647N is also distinctly separated from the yellow LED emission spectrum. The DNA sequences and their names used in the study of IHF-DNA binding are listed in Table 1S in the Supporting Information. The dsDNA molecules were hybridized at 30 μM in 150 mM sodium phosphate buffer, made with DI water, sodium phosphate monobasic, and sodium phosphate bibasic powder (Sigma-Aldrichm MO).

Measurements of DNA conformation and IHF-DNA binding were made in 10 mM Tris, 50 mM NaCl, and 10 mg/mL bovine serum albumin (BSA) buffer prepared with Tris buffered saline tablets, NaCl powder, and BSA powder (Sigma-Aldrich, MO) unless specified. All buffer solutions were prepared with deionized water (DI water) filtered by Barnstead Nanopure Diamond (18.2 $M\Omega/cm^{-1}$ resistance, Thermo Scientific, Waltham, MA). Biosensor substrates were prepared from silicon wafers with 17.5 μm thick thermally grown oxide layer (Silicon Valley Microelectronics, Santa Clara, CA), which were cut into 15 mm × 15 mm square sensor chips. Before use, chips were rinsed with acetone, methanol, and subjected to sonication in acetone for 5 min, and oxygen plasma ashing (M4LTM, PVA TePla America, Corona, CA) for 10 min. DNA microarray spotting and surface functionalization of the biosensor substrate with a polymeric coating were prepared in the same fashion as previously described[24]. The average diameter of the DNA spots ranges from 120 μm to 150 μm, which determines the pitch between the DNA spots. In the experiments presented in this paper, a pitch of the DNA spots was set to be 300 μm. Under the current design of the flow cell and the DNA microarray, about a total of 750 DNA spots (50 rows of DNA spots with 15 DNA spots per row) can be evaluated in one experiment.

Wild-type integration host factor (IHF) protein of Escherichia coli was a gift from Prof. Peter Dröge at Nanyang Technological University. IHF was stored in 10 mM Tris-HCl buffer at pH 7.6, containing 50 mM NaCl and 30% glycerol. IHF stock solution was immediately stored in –30° freezer after shipping from Singapore to Boston University. Sodium dodecyl sulfate polyacrylamide gel electrophoresis (SDS-PAGE) assay was performed on 4-20% gradient Polyacrylamide Mini-PROTEAN® TGX™ Precast Gels (Bio-Rad, Hercules, CA) regularly to check the integrity and purity of the protein before each experiment (See Supporting Information, Figure 1S). The average concentration of the stock IHF solution was determined to be 83.2 μM from Bradford protein assays using NanoDrop 2000c UV-Vis Spectrophotometer (Thermal Scientific, Wilmington, DE, see Supporting Information, Figure 2S).

For each binding experiment, at first, the binding buffer containing 10 mM Tris and 50 mM NaCl without IHF and BSA was first flowed through the flow cell for 5 minutes to immerse the DNA microarray in the solution. Then, the heights of fluorophores attached to the surface-distal and surface proximal ends of the dsDNA were measured by SSFM. Second, the binding buffer without IHF but with 10 mg/mL BSA was flowed through the flow cell for 10 minutes to block the background of the microarray surface and reduce non-specific binding of IHF to the background. Then, the binding buffer solutions with increasing concentrations of IHF were driven the through the inlet and outlet of the flow cell sequentially using a peristaltic pump. For each IHF binding solution with a particular IHF concentration, after an estimated period of time for IHF binding to reach equilibrium, repetitive SSFM and WLRS spectral measurements were made and the measured data were processed in real-time until the processed results reached equilibrium. An exemplary real-time measurement of average fluorophore height change in a

separate experiment is included in section 7 in the Supporting Information to provide a sense of scale for the time required for the IHF binding reaction to reach equilibrium.

3. Additive Langmuir binding isotherm model

We used a generalized additive Langmuir binding isotherm model to decouple the specific and non-specific binding modes of IHF to DNA measured by WLRS. The additive model adds two adapted Langmuir binding isotherms, one describing specific binding of IHF to DNA, the other describing nonspecific binding of IHF to DNA:

$$\langle R \rangle = \langle R_{specific} \rangle \frac{x}{K_{d(specific)} + x} + \langle R_{nonspecific} \rangle \frac{x}{K_{d(nonspecific)} + x}$$

where $\langle R \rangle$ is the measured average IHF to DNA binding ratio, x is the IHF concentration in binding buffer solution; $K_{d(specific)}$ is the dissociation constant of specific IHF binding to the DNA sequence, and is obtained from fitting the equilibrium binding isotherms of the average fluorophore height change to a single adapted Langmuir binding isotherm model; $K_{d(nonspecific)}$ is the dissociation constant of nonspecific IHF binding to the DNA sequence; $\langle R_{specific} \rangle$ is the maximum average ratio of IHF specifically bound to DNA at equilibrium, and $\langle R_{nonspecific} \rangle$ is the maximum average ratio of IHF nonspecifically bound to DNA at equilibrium.

CONCLUSION

We present a high-throughput imaging biosensor platform combining two interferometric sensing techniques, WLRS and SSFM, to quantify DNA conformational change and protein-DNA binding in a DNA microarray format. SSFM allows for measurement of DNA conformational change by determining height changes of fluorophores tagged to specific nucleotides of surface-immobilized DNA molecules. WLRS allows for quantitation of surface

molecular density independent of surface conformation by measuring optical thicknesses of accumulated biomolecules on the surface. By implementing a dual-spectral imaging configuration, we combined and implemented the two different techniques in one optical setup by using two spectral bandwidths simultaneously, each corresponding to an independent quantitative measurement. Using the *E. coli* integration host factor protein as the molecular model system, we demonstrated quantitative characterization of conformational specific protein-DNA interaction. The imaging biosensor platform can be readily combined with high-throughput protein-binding microarray technologies for systematic and comprehensive investigation of conformational specific protein-DNA interactions.

However, any technique alone cannot equip us with all the information needed to elucidate protein-DNA interactions and their functions in the complex crowded cellular environment. The capabilities of the imaging biosensor platform can be additionally combined with other *in vivo*, *in vitro*, and computational techniques. For example, computational prediction and high-throughput experimental measurements of protein-DNA interactions can be performed iteratively to study the specific binding mechanisms of a selected conformational specific protein-DNA complexes, whose structures can be further analyzed by X-ray crystallography or NMR spectroscopy at the atomic scale. Alternatively or additionally, the functions of these selected protein-DNA complexes can be examined by site-specific mutagenesis studies in the cell to understand their regulatory roles *in vivo*. Eventually, a workflow that includes iterative computational binding site prediction and high-throughput conformational specificity analysis, followed up by crystal structure characterization and *in vivo* functional studies might serve as a viable and collaborative approach to discover the missing components of protein-DNA interactions.

Supporting Information. DNA sequences and nomenclature (Table 1S); SDS-PAGE assay of IHF stock solution (Figure 1S); determination of the concentration of IHF stock solution by Bradford assay (Figure 2S); equilibrium binding isotherm fitting results of other DNA sequences (Table 2S); calculation of dissociation constants (Figure 3S, Figure 4S; Table 2S); geometric model for quantitation of DNA bending angle induced by specific IHF binding (Figure 4S); customized flow cell assembly (Figure 5S); real-time measurement of average fluorophore height change by SSFM (Figure 6S); summary of binding parameters obtained from additive isotherm model fitting (Table 3S); average surface densities of 10 dsDNA spots and bound IHF at equilibrium (Table 4S); effects of surface densities on the binding and bending of dsDNA (Tables 5S and 6S, Figures 7S-10S). This material is available free of charge via the Internet at http://www.rsc.org.

REFERENCES

1. P. H. von Hippel and J. D. McGhee, *Annu. Rev. Biochem.*, 1972, **41**, 231–300.
2. P. H. von Hippel, *Annu. Rev. Biophys. Biomol. Struct.*, 2007, **36**, 79–105.
3. C. Bernstein, A. R. Prasad, V. Nfonsam, and H. Bernstein, *New Research Directions in DNA Repair*, 2013, 413–465.
4. T. J. Richmond and C. A. Davey, *Nature*, 2003, **423**, 145–150.
5. G. D. Stormo and Y. Zhao, *Nature Reviews Genetics*, 2010, **11**, 751–760.
6. R. Rohs, X. Jin, S. M. West, R. Joshi, B. Honig, and R. S. Mann, *Annu. Rev. Biochem.*, 2010, **79**, 233–269.
7. S. Mukherjee, M. F. Berger, G. Jona, X. S. Wang, D. Muzzey, M. Snyder, R. A. Young, and M. L. Bulyk, *Nat Genet*, 2004, **36**, 1331–1339.
8. M. L. Bulyk, *Current Opinion in Biotechnology*, 2006, **17**, 422–430.
9. M. F. Berger, A. A. Philippakis, A. M. Qureshi, F. S. He, P. W. Estep, and M. L. Bulyk, *Nature Biotechnology*, 2006, **24**, 1429–1435.
10. M. F. Berger and M. L. Bulyk, *Nat Protoc*, 2009, **4**, 393–411.
11. M. A. Hume, L. A. Barrera, S. S. Gisselbrecht, and M. L. Bulyk, *Nucleic Acids Research*, 2015, **43**, D117–D122.
12. A. Zykovich, I. Korf, and D. J. Segal, *Nucleic Acids Research*, 2009, **37**, e151–e151.
13. M. Garber, N. Yosef, A. Goren, R. Raychowdhury, A. Thielke, M. Guttman, J. Robinson, B. Minie, N. Chevrier, Z. Itzhaki, R. Blecher-Gonen, C. Bornstein, D. Amann-Zalcenstein, A. Weiner, D. Friedrich, J. Meldrim, O. Ram, C. Cheng, A. Gnirke, S. Fisher, N. Friedman, B. Wong, B. E. Bernstein, C. Nusbaum, N. Hacohen, A. Regev, and I. Amit,

Molecular Cell, 2012, **47**, 810–822.
14. R. Blecher-Gonen, Z. Barnett-Itzhaki, D. Jaitin, D. Amann-Zalcenstein, D. Lara-Astiaso, and I. Amit, *Nat Protoc*, 2013, **8**, 539–554.
15. S. Jones, P. van Heyningen, H. M. Berman, and J. M. Thornton, *Journal of Molecular Biology*, 1999, **287**, 877–896.
16. R. Rohs, S. M. West, A. Sosinsky, P. Liu, R. S. Mann, and B. Honig, *Nature*, 2009, **461**, 1248–1253.
17. R. Rohs, S. M. West, P. Liu, and B. Honig, *Current Opinion in Structural Biology*, 2009, **19**, 171–177.
18. A. Marcovitz and Y. Levy, *Proceedings of the National Academy of Sciences*, 2011, **108**, 17957–17962.
19. P. Vivas, Y. Velmurugu, S. V. Kuznetsov, P. A. Rice, and A. Ansari, *Journal of Molecular Biology*, 2012, **418**, 300–315.
20. R. P. C. Driessen, G. Sitters, N. Laurens, G. F. Moolenaar, G. J. L. Wuite, N. Goosen, and R. T. Dame, *Biochemistry*, 2014, **53**, 6430–6438.
21. L. Moiseev, C. R. Cantor, M. I. Aksun, M. Dogan, B. B. Goldberg, A. K. Swan, and M. S. Ünlü, *J. Appl. Phys.*, 2004, **96**, 5311.
22. A. Yalçın, F. Damin, E. Ozkumur, G. di Carlo, B. B. Goldberg, M. Chiari, and M. S. Ünlü, *Anal. Chem.*, 2009, **81**, 625–630.
23. P. S. Spuhler, L. Sola, X. Zhang, M. R. Monroe, J. T. Greenspun, M. Chiari, and M. S. Ünlü, *Anal. Chem.*, 2012, **84**, 10593–10599.
24. X. Zhang, G. G. Daaboul, P. S. Spuhler, D. S. Freedman, A. Yurt, S. Ahn, O. Avci, and M. S. Ünlü, *Analyst*, 2014, **00**, 1–10.
25. L. Moiseev, M. S. Ünlü, A. K. Swan, B. B. Goldberg, and C. R. Cantor, *Proceedings of the National Academy of Sciences*, 2006, **103**, 2623–2628.
26. M. Zavali, P. S. Petrou, S. E. Kakabakos, M. Kitsara, I. Raptis, K. Beltsios, and K. Misiakos, *Micro Nano Lett.*, 2006, **1**, 94.
27. P. S. Petrou, D. Ricklin, M. Zavali, I. Raptis, S. E. Kakabakos, K. Misiakos, and J. D. Lambris, *Biosensors and Bioelectronics*, 2009, **24**, 3359–3364.
28. M. Kitsara, P. Petrou, D. Kontziampasis, K. Misiakos, E. Makarona, I. Raptis, and K. Beltsios, *Microelectronic Engineering*, 2010, **87**, 802–805.
29. D. Singh Mehta and V. Srivastava, *Appl. Phys. Lett.*, 2012, **101**, 203701.
30. C. Yu, C. A. Lopez, H. Hu, Y. Xia, D. S. Freedman, A. P. Reddington, G. G. Daaboul, M. S. Ünlü, and C. A. Genco, *PLoS ONE*, 2014, **9**, e96832.
31. P. A. Rice, S. Yang, K. Mizuuchi, and H. A. Nash, *Cell*, 1996, **87**, 1295–1306.
32. T. Ellenberger and A. Landy, *Structure*, 1997, **5**, 153–157.
33. J. A. Holbrook, O. V. Tsodikov, R. M. Saecker, and M. T. Record Jr, *Journal of Molecular Biology*, 2001, **310**, 379–401.
34. K. A. Vander Meulen, R. M. Saecker, and M. T. Record Jr, *Journal of Molecular Biology*, 2008, **377**, 9–27.
35. D. F. Browning and S. J. W. Busby, *Nat Rev Micro*, 2004, **2**, 57–65.
36. U. Rant, K. Arinaga, S. Fujita, N. Yokoyama, G. Abstreiter, and M. Tornow, *Langmuir*, 2004, **20**, 10086–10092.
37. P. Spuhler, X. Zhang, M. Monroe, J. Greenspun, M. S. Ünlü, L. Sola, and M. Chiari, 2011, pp. 91–92.
38. M. Castronovo, S. Radovic, C. Grunwald, L. Casalis, M. Morgante, and G. Scoles, *Nano*

Lett., 2008, **8**, 4140–4145.
39. T. W. Lynch, E. K. Read, A. N. Mattis, J. F. Gardner, and P. A. Rice, *Journal of Molecular Biology*, 2003, **330**, 493–502.
40. E. K. Read, *Journal of Biological Chemistry*, 2000, **275**, 33759–33764.
41. E. Ozkumur, A. Yalçın, M. Cretich, C. A. Lopez, D. A. Bergstein, B. B. Goldberg, M. Chiari, and M. S. Ünlü, *Biosensors and Bioelectronics*, 2009, **25**, 167–172.
42. G. G. Daaboul, R. S. Vedula, S. Ahn, C. A. Lopez, A. Reddington, E. Ozkumur, and M. S. Ünlü, *Biosensors and Bioelectronics*, 2011, **26**, 2221–2227.
43. M. Ritzefeld and N. Sewald, *Journal of Amino Acids*, 2012, **2012**, 1–19.
44. T. M. Squires, R. J. Messinger, and S. R. Manalis, *Nature Biotechnology*, 2008, **26**, 417–426.
45. B. J. Ali, R. Amit, I. Braslavsky, A. B. Oppenheim, O. Gileadi, and J. Stavans, *Proceedings of the National Academy of Sciences*, 2001, **98**, 10658–10663.
46. J. Lin, H. Chen, P. Dröge, and J. Yan, *PLoS ONE*, 2012, **7**, e49885.
47. O. V. Tsodikov, J. A. Holbrook, I. A. Shkel, and M. T. Record Jr, *Biophysj*, 2001, **81**, 1960–1969.
48. G. M. Dhavan, D. M. Crothers, M. R. Chance, and M. Brenowitz, *Journal of Molecular Biology*, 2002, **315**, 1027–1037.
49. P. S. Spuhler, J. Knezevic, A. Yalcin, Q. Bao, E. Pringsheim, P. Droge, U. Rant, and M. S. Ünlü, *Proceedings of the National Academy of Sciences*, 2010, **107**, 1397–1401.
50. C. Zhu, K. J. R. P. Byers, R. P. McCord, Z. Shi, M. F. Berger, D. E. Newburger, K. Saulrieta, Z. Smith, M. V. Shah, M. Radhakrishnan, A. A. Philippakis, Y. Hu, F. De Masi, M. Pacek, A. Rolfs, T. Murthy, J. LaBaer, and M. L. Bulyk, *Genome Research*, 2009, **19**, 556–566.
51. S. A. Jaeger, E. T. Chan, M. F. Berger, R. Stottmann, T. R. Hughes, and M. L. Bulyk, *Genomics*, 2010, **95**, 185–195.
52. R. Gordân, K. F. Murphy, R. P. McCord, C. Zhu, A. Vedenko, and M. L. Bulyk, *Genome Biol*, 2011, **12**, R125.